

1 Break in precipitation – temperature scaling over India 2 predominantly explained by cloud-driven cooling

3 Sarosh Alam Ghausi^{1,2}, Subimal Ghosh^{3,4} and Axel Kleidon¹
4
5

6 ¹ Biospheric Theory and Modelling Group, Max Planck Institute for Biogeochemistry, Jena 07745,
7 Germany.

8 ² International Max Planck Research School for Global Biogeochemical Cycles (IMPRS – gBGC), Jena
9 07745, Germany

10 ³ Department of Civil Engineering, Indian Institute of Technology Bombay 400076, India

11 ⁴ Interdisciplinary Programme in Climate Studies, Indian Institute of Technology Bombay 400076, India

12 *Correspondence to:* Sarosh Alam Ghausi (sghausi@bgc-jena.mpg.de)
13

14 **Abstract.** Climate models predict an intensification of precipitation extremes as a result of a warmer and
15 moister atmosphere at the rate of 7%/K. However, observations in tropical regions show contrastingly
16 negative precipitation-temperature scaling at temperatures above 23° - 25°C. We use observations from
17 India and show that this negative scaling can be explained by the radiative effects of clouds on surface
18 temperatures. Cloud radiative cooling during precipitation events make observed temperatures co-vary
19 with precipitation, with wetter periods and heavier precipitation having a stronger cooling effect. We
20 remove this confounding effect of clouds from temperatures using a surface energy balance approach
21 constrained by thermodynamics. We then find a diametric change in precipitation scaling with rates
22 becoming positive and coming closer to the Clausius – Clapeyron scaling rate (7%/K). Our findings imply
23 that the intensification of precipitation extremes with warmer temperatures expected with global warming
24 is consistent with observations from tropical regions when the radiative effect of clouds on surface
25 temperatures and the resulting covariation with precipitation is accounted for.
26

27 **1 Introduction**

28 Climate models and observed trends have shown precipitation extremes to increase at the global scale
29 with anthropogenic global warming (Fischer et al., 2013; Westra et al., 2013; Donat et al., 2016). This
30 increase is largely explained by the thermodynamic Clausius-Clapeyron (CC) equation, suggesting a
31 $\approx 7\%/K$ increase in atmospheric moisture holding capacity per degree rise in temperature ("CC rate")
32 (Allen & Ingram, 2002). Extreme precipitation is expected to increase at a similar rate (Trenberth et al.,
33 2003; Held & Soden., 2006; O’Gorman & Schneider, 2009), as also shown by convection-permitting
34 climate model projections (Kendon et al., 2014; Ban et al., 2015). Precipitation – temperature scaling
35 rates, estimated using statistical methods and observed records, are widely used as an indicator to
36 constrain this response (Lenderink et al., 2008; Wasko et al, 2014).

37
38 However, observed scaling rates show large heterogeneity globally, with significant deviations from the
39 CC rate (Westra et al., 2014; Schroeer & Kirchengast, 2018). Deviations are larger in the tropical regions
40 where scaling rates are mostly negative and precipitation extremes largely show a monotonic decrease or
41 a sudden drop (hook) in scaling at high temperatures (Utsumi et al., 2011). These deviations have been
42 studied and attributed to number of factors. Two primarily argued reasons include the moisture
43 availability limitation at high temperatures (Hardwick et al., 2010) and dependence of scaling estimates
44 on the wet event duration (Gao et al., 2018; Ghausi & Ghosh 2020; Visser et al., 2021). Cooling effects
45 of rainfall events have also questioned the use of surface air temperature as scaling variable (Bao et al.,
46 2017). Other scaling variables like atmospheric air temperature (Golroudbary et al., 2019), sampling
47 temperatures before the start of storm (Visser et al., 2020), using measures of atmospheric moisture like
48 dew point temperature (Bui et al., 2019) and integrated water vapor (Roderick et al., 2019) have been
49 suggested as an alternative to surface air temperatures. The use of atmospheric moisture as a scaling
50 variable has been criticized because it provides less insight about precipitation sensitivity to temperature
51 and is also not entirely immune to cooling effects of rainfall (Bao et al., 2018). Other factors that can
52 cause deviations in scaling includes the change in rainfall type from stratiform to convective (Berg et al.,
53 2013; Molnar et al., 2015) and seasonality in precipitation (Sun et al., 2020). Owing to these uncertainties,

54 the use of scaling relationships derived from observations to infer future changes in extreme precipitation
55 in these regions remains debatable.

56

57 In this study, we show that a large part of uncertainties in this response and negative scaling rates in the
58 tropics are mainly caused by the radiative effect of clouds on surface temperatures. Precipitation events
59 are accompanied by strong cloud cover, which reduces the solar absorption at the surface and hence
60 lowers surface temperatures. This radiative cooling associated with precipitation can be significant in the
61 tropical regions where insolation and temperatures are high. As a result, regions and periods of more
62 intense precipitation cool more, and this affects their position in the scaling curve. This implies that
63 temperature observations are not independent of precipitation and this dependency obscures their scaling
64 relationship. We used a thermodynamic systems approach to remove this cooling effect from surface
65 temperatures. We then show that when this effect is being removed, no breakdown in the scaling
66 relationship is seen in observations and extreme precipitation then scales positively with temperature
67 close to CC rate.

68

69 To remove the effects of clouds, we used a surface energy balance formulation in conjunction with the
70 first and second law of thermodynamics (Kleidon & Renner, 2013). This approach provides us with
71 additional thermodynamic constraints on the turbulent flux exchange between surface and atmosphere.
72 We used this thermodynamically constrained model and force it with the “all-sky” and “clear-sky”
73 radiative fluxes. These fluxes are a standard product in NASA-CERES radiation datasets such that “all-
74 sky” fluxes are representative of observed conditions including the cloud effects while “clear-sky” fluxes
75 are diagnosed by removing the effect of clouds from the radiative transfer. Compounding the
76 thermodynamic constraint on turbulent fluxes together with the radiative fluxes helps us to estimate “all-
77 sky” and “clear-sky” temperatures that includes and excludes the radiative effects of clouds respectively.

78

79 We then evaluate this effect and its impact on precipitation-temperature scaling using observations from
80 India. India is a tropical country where the extreme precipitation and the resulting floods have intensified
81 over the past years (Goswami et al., 2006) and are expected to increase in the future (Katzenberger et al.,

Deleted: Here

Deleted: Here w

84 2021). However, extreme precipitation–temperature scaling is largely negative over most of India (Vittal
85 et al., 2016; Sharma et al., 2019), which is in contrast to the observed trends (Roxy et al., 2017). **In this**
86 **study, we attempt to resolve this inconsistency in precipitation – temperature scaling by removing the**
87 cloud cooling effects from surface temperatures. To do this, we use gridded precipitation – temperature
88 datasets that were used in previous studies (Vittal et al., 2016; Mukherjee et al., 2018; Sharma et al., 2019;
89 Ghausi et al., 2020) and supplement it with the gridded radiative flux datasets to remove the cloud
90 radiative effects. More details on our surface energy-balance model and estimation of surface
91 temperatures “with” and “without” clouds are followed in the section 2.1 with the details of datasets being
92 used in section 2.2. We used these reconstructed temperatures to study the effect of clouds on precipitation
93 – temperature scaling over India. To estimate the precipitation – temperature scaling rates, we used the
94 widely adopted statistical methods. Details of them are further provided in section 2.3. Results are then
95 presented and discussed in section 3.

Deleted: We here

96 **2 Methods and Data**

97 **2.1 Thermodynamically constrained energy balance model**

98 To infer surface temperatures from the radiative forcing and remove the effects of clouds, we start with a
99 simple physical formulation of the surface energy balance. The surface of the Earth is heated by solar
00 absorption and downwelling longwave radiation. This heat is released back to the atmosphere through
01 surface emission of longwave radiation and exchange of turbulent fluxes of sensible and latent heat. This
02 balance between the incoming and outgoing energy fluxes at the Earth’s surface is described by equation
03 (1).

Deleted: the

$$04 \quad R_s + R_{l,down} = R_{l,up} + J \quad (1)$$

05 Here R_s is the surface net solar absorption, R_{ld} is the downwelling longwave radiation, $R_{l,up}$ is the
06 upwelling longwave radiation emitted from the surface and J is turbulent flux exchange between surface
07 and the atmosphere (comprising of sensible and latent heat). We neglect the ground heat flux, as it is
08 generally small when averaged over a few days or longer. While R_s and $R_{l,down}$ can be obtained using
09 radiation datasets for different sky conditions, the partitioning between $R_{l,up}$ and J is poorly constrained
10 by surface energy balance alone. To have these additional constraints on J , we used a thermodynamic

Deleted: d

14 systems approach to view the earth system. Similar approach had also been used in (Kleidon & Renner,
15 2013; Kleidon et al., 2014; Dhara et al., 2016) and were found to very well capture the observed surface
16 temperatures, energy partitioning and climate sensitivities.

17 To do this, we conceptualize the surface atmosphere system as a heat engine, with warm Earth surface as
18 the heat source and cooler atmosphere being the sink (Figure 1). Heat and mass are transported within
19 this engine by the exchange of turbulent fluxes (J) between the surface and the atmosphere. The
20 differential radiative heating and cooling between the surface and the atmosphere maintains the
21 temperature difference and drives the vertical convective motion. The power (G) associated with the work
22 done by the heat engine required to sustain convective motion in form of vertical mixing and exchange
23 of turbulent fluxes can be derived simply using the first and second law of thermodynamics and can be
24 represented by the well-established Carnot limit as

$$G = J \left(1 - \frac{T_a}{T_s} \right). \quad (2)$$

25 Detailed derivation about [this](#) can be found in (Kleidon & Renner, 2013; Kleidon et al., 2014). Here T_a
26 and T_s are the representative temperatures of cold atmosphere and the hot surface respectively.

Deleted: the same

28 Both temperatures are inferred from their respective energy balances. The atmospheric temperature (T_a)
29 is assumed to be equal to the radiative temperature of atmosphere (T_r) and is estimated using the outgoing
30 longwave radiation at top of atmosphere ($R_{l,toa}$)

$$T_a = \left(\frac{R_{l,toa}}{\sigma} \right)^{1/4}. \quad (3)$$

31 Here, σ is the Stefan Boltzmann constant ($\sigma = 5.67 \times 10^{-8} \text{ Wm}^{-2}\text{K}^{-4}$). A correction of 15K was applied to
32 the radiative temperature to account for the assumption of black atmosphere and effective height of
33 convection (Dhara et al., 2016). We consider the atmosphere as opaque to terrestrial radiation and hence
34 it is assumed that all outgoing longwave radiation emitted into space originates from the atmosphere.

36 The heat engine source temperature i.e. surface temperature (T_s) can be expressed from the emitted
37 longwave radiation from the surface ($R_{l,up}$) as

$$T_s = \left(\frac{R_{l,up}}{\sigma} \right)^{1/4}. \quad (4)$$

40 Using the surface energy balance (Eq. 1), we can then express the surface temperature in terms of net
41 solar absorption, downwelling longwave radiation and turbulent fluxes (J) as

$$42 \quad T_s = \left(\frac{R_s + R_{l,down} - J}{\sigma} \right)^{1/4}. \quad (5)$$

43 The differential radiative heating and cooling between the surface and the atmosphere maintains the
44 temperature difference and drives the vertical convective motion. Thermodynamics sets a limit to this
45 conversion and thus constrains the amount of turbulent flux exchange. Less turbulent fluxes result in a
46 hotter surface (Eq. 5), which will increase the temperature difference between the surface and atmosphere.
47 This will subsequently increase the efficiency term in the generation rate, the second term on the right-
48 hand side of Eq. (2). On the other hand, an increase in turbulent fluxes (J) increases the first term in the
49 generation rate of Eq. (2), but it will, in turn, reduce the surface temperature and temperature difference
50 between surface and atmosphere (Eq. 5). Thus, there exists a trade-off that sets the limit for the power to
51 maintain vertical energy and mass exchange between surface and the atmosphere. This limit is termed as
52 the maximum power limit and provides an additional constraint to surface energy balance partitioning
53 that we used here to infer surface temperatures.

54 Using Equations. (2), (3) and (5), the rate of work done (power) produced by the heat engine can be
55 expressed as a function of turbulent fluxes (J) as

$$56 \quad G = J \left(1 - T_a \left(\frac{R_s + R_{l,down} - J}{\sigma} \right)^{-1/4} \right). \quad (6)$$

57 Note that power $G = 0$ when $J = 0$ or when $J = R_s + R_{l,down} - R_{l,toa}$. Hence, there is a maximum $G_{max} = G$
58 ($J_{maxpower}$) for a value between $0 < J_{maxpower} < R_s + R_{l,down} - R_{l,toa}$. The optimum J that maximizes power
59 was calculated numerically. This flux was then used to determine the surface temperatures.

$$60 \quad T_{s,maxpower} = \left(\frac{R_s + R_{l,down} - J_{maxpower}}{\sigma} \right)^{1/4} \quad (7)$$

61 Surface temperatures were estimated using Eq. 7 for “all-sky” and “clear-sky” radiative conditions using
62 radiative forcing from the NASA – CERES datasets. We then refer to these two temperatures derived
63 using Eq. 7 as “all-sky” and “clear-sky” temperatures.

64
65

71 **2.2 Datasets used**

72 Radiative fluxes of shortwave and longwave radiation at surface and top of atmosphere (TOA) were
73 obtained from the NASA - CERES (EBAF 4.1) dataset (Loeb et al., 2018; Kato et al., 2018) and NASA
74 CERES Syn1deg dataset (Doelling et al., 2013,2016). These datasets are available for both “all-sky” as
75 well as “clear-sky” conditions at monthly and daily scale respectively with a 1° latitude x 1° longitude
76 spatial grid resolution and were used as a forcing in our energy balance model. We evaluated our model
77 using observations derived gridded temperature data from Indian Meteorological Department (IMD,
78 Rajeevan et al., 2008). To estimate the precipitation – temperature scaling, we used daily gridded
79 precipitation and temperature datasets with a spatial resolution of 1° latitude x 1° longitude from the
80 Indian Meteorological Department (IMD, Rajeevan et al., 2008) and 3 hourly gridded rainfall data from
81 NASA-TRMM_3B42 with a spatial resolution of 0.25° x 0.25°. We repeated the analysis using daily
82 gridded precipitation and temperature data from the APHRODITE (Asian Precipitation Highly Resolved
83 Observational Data Integration towards Evaluation) dataset, available at a spatial resolution of 0.25° x
84 0.25° (Yatagai et al., 2012). To further ensure robustness of our results, we also used 3 station-based daily
85 precipitation – temperature observations in India (Mumbai Airport, Bangalore Airport and Chennai
86 Airport) from global surface summary of the day (GSOD) data provided by National Oceanic and
87 Atmospheric Administration (NOAA). Daily dew point temperatures were obtained from the ERA-5
88 reanalysis. Based on the availability of all datasets, the period of analysis was chosen from the years 2003
89 to 2015.

90

91 **2.3 Estimation of precipitation – temperature scaling rates**

92 Extreme precipitation events were scaled with observed, “all-sky” and “clear-sky” temperatures using
93 two widely adopted scaling approaches: The Binning Method (Lenderink et al., 2008) and Quantile
94 Regression (Wasko et al., 2014). For the binning method, we defined extreme precipitation events using
95 a threshold of 99th percentile precipitation contained at each grid cell. Precipitation – temperature pairs
96 were then divided into the increasing order of non-overlapping bins of 2 K width. Only those bins which
97 have at least 150 data points have been considered for the analysis (Utsumi et al., 2011). The median
98 value of each bin was then used to examine the variation of precipitation extremes with temperature. Bins

99 with temperature less than 3°C were discarded to remove the effects of freezing, thawing and snowfall.
100 To ensure that our results are not biased with the number of data points in each bin and bin sizes (which
101 may affect the nature of the scaling relationship), we further used the Quantile Regression method to
102 estimate the scaling rates.

103 Quantile regression estimates the conditional quantile of the dependent variable (in our case,
104 precipitation) over the given values of the independent variable (temperature). We first fitted a quantile
105 regression model between the logarithmic precipitation and temperature values at the target quantile of
106 99%

$$107 \quad \text{Log}(P_i) = \beta_o^{99} + \beta_1^{99}(T_i) \quad . \quad (8)$$

108 Here P_i denotes the mean daily precipitation intensity and T_i is the daily mean temperature, and β_o^{99} and
109 β_1^{99} are the regression coefficients for the 99th quantile of precipitation. The slope coefficient β_1^{99} is then
110 exponentially transformed to estimate the scaling rate (α_1).

$$111 \quad \alpha_1 = 100 \cdot (e^{\beta_1^{99}} - 1) \quad (9)$$

112 The ~~forementioned~~ methodology had been widely adopted to estimate the extreme precipitation –
113 temperature scaling in previous studies (Lenderink et al., 2008, 2010; Utsumi et al., 2011; Wasko et al.,
114 2014; Schroeer et al., 2018).

Deleted: following

115 **3 Results and Discussion**

116 In this section, we first start by a quick evaluation of our thermodynamic approach by comparing the
117 estimated “all-sky” temperatures against observations. We then quantify the cloud radiative effects on
118 surface temperatures and check for its spatial consistency across regions. We then estimated precipitation
119 – temperature scaling rates by including and excluding the effect of clouds on surface temperatures. We
120 also used dew point temperature (a proxy measure for atmospheric moisture) as a scaling variable. Later,
121 we discuss our interpretation of scaling by excluding cloud effects from temperatures, its comparison with
122 the dew point scaling and its implications across regions.

123
124

26 **3.1: Evaluating the modelled temperatures**

27 “All-sky” temperatures were estimated using the daily observed radiative fluxes from CERES in
28 conjunction with surface energy partitioning constrained by maximum power (see Equation 7). We found
29 an extremely good agreement of these estimated temperatures when compared to surface temperature
30 observations over India with $R^2 > 0.9$ and $RMSE < 1.5$ K over most regions (Figure 2). This signifies that
31 our formulation strongly captures the surface temperature variation over India and thus validates our
32 approach. We then extend this for clear-sky conditions by forcing our model with “clear-sky” radiative
33 fluxes from CERES and estimating “clear-sky” temperatures. It is to note that “clear-sky” temperatures
34 are reconstructed temperatures estimated by removing the effect of clouds from radiative transfer.

35 **3.2: Estimating the cloud radiative cooling**

36 We used the difference between the “all-sky” and “clear-sky” temperatures as a measure to quantify the
37 effect of cloud-driven cooling during rainfall events. This cooling increases strongly with precipitation
38 across regions, resulting in a stronger reduction in surface temperature with greater precipitation (Figure
39 3a). This cooling is predominantly caused by the substantial reduction in absorbed solar radiation at the
40 surface for “all-sky” conditions compared to “clear-sky” conditions (Figure 3b). On the other hand,
41 changes in longwave radiation are comparatively small and largely remain insensitive to precipitation.
42 To examine the spatial consistency in precipitation variability and associated cooling, we isolated extreme
43 daily precipitation days over each grid. Figure 4a shows the mean magnitude of daily extreme
44 precipitation events over India. The pattern was consistent with the cloud cover map from NASA-CERES
45 (shown in Appendix C). Figure 4b shows the cloud-cooling associated with these days. This cooling effect
46 of clouds and precipitation shows a clear, systematic variation across India. The cooling effect is greater
47 where precipitation rates are high. In contrast, in the more arid regions in the northwest of India, the
48 cooling effect almost disappears with low precipitation rates. In the Northernmost Himalayan region, the
49 difference in “clear-sky” and “all-sky” temperatures is negative. These high-altitude regions are more
50 sensitive to changes in longwave radiations. As a result, there is a significant increase in longwave
51 radiation with increase in cloud cover which compensates for the cooling due to reduction in shortwave
52 over those grids. Figure 4c further shows the mean “all-sky” temperature during these days. We find that
53 the heaviest events occur at a relatively lower temperature as a result of stronger cooling. Figure 4d shows

54 the mean number of rainfall days per year. More rainy days implies more cloudy conditions and thus a
55 stronger cloud radiative cooling over that region. Having quantified this effect of cloud radiative cooling
56 and its systematic variation across regions, we then estimate its impact on the precipitation – temperature
57 scaling.

58

59 **3.3 Impact on precipitation-temperature scaling**

60 We performed a binning analysis (Lenderink et al., 2008) to understand the scaling of precipitation
61 extremes with temperature using observed temperatures as well as our estimated "clear-sky" and "all-sky"
62 temperatures. Precipitation events were isolated and binned into P-T pairs and the resulting scaling
63 relationships are shown in Figure 5. The scaling relationship using observed and "all-sky" temperatures
64 showed similar scaling behaviour (yellow and red lines in Figure 5a). Extreme precipitation increases
65 close to the CC rate up to a threshold of around 23° - 24°C, above which the scaling becomes negative.
66 This break in scaling behaviour with observed temperatures is consistent with the findings of previous
67 studies (Hardwick et al., 2010; Ghausi & Ghosh, 2020) and is commonly referred in literature as "hook"
68 or "peak structure" (Wang et al., 2017; Gao et al., 2018). However, when precipitation extremes are scaled
69 with "clear-sky" temperatures that excludes the cloud-cooling effect, the resulting scaling relationship
70 does not show a breakdown and increases consistently, close to the CC rate over the whole temperature
71 range (blue line in Fig. 5a). Similar results were obtained when the scaling curves were reproduced for
72 station-based observations (See Appendix A).

73 Previous studies (Hardwick et al., 2010; Chan et al., 2015; Wang et al., 2017) have attributed the break
74 in precipitation-temperature scaling to a lack of moisture availability as relative humidity tends to
75 decrease at high temperatures. To account for this effect of moisture limitation, some studies used dew
76 point temperature, a measure of atmospheric humidity, as an alternative scaling variable (Wasko et al.,
77 2018; Barbero et al., 2018). They showed that the breakdown and negative scaling disappear when scaled
78 with dew point temperatures (Zhang et al., 2019; Ali et al., 2021). To evaluate this interpretation and
79 compare it to ours, we used the dew point temperature from the ERA-5 reanalysis. We derived the extreme
80 precipitation scaling using this temperature (Figure 5b) and compared it to our "all-sky" and "clear-sky"
81 temperatures (Figure 5c).

82 At first sight, the scaling relationship using dew point temperatures looks very similar to our "clear-sky"
83 relationship (compare Figures 5a and 5b, but note the difference in temperature scale). Yet, its
84 interpretation differs because using dew point temperatures merely implies that the intensity of extreme
85 precipitation events scales with the moisture content of the air, with moister air resulting in higher
86 intensity events. Dew point scaling thus carries less insight about the response of extreme precipitation to
87 climate warming (Bao et al., 2018). To infer the precipitation sensitivity with temperature from dew point
88 scaling, one then needs to see how dew point temperatures change with actual temperatures (dT_{dew}/dT)
89 (Figure 5c). This is further demonstrated using equation 10.

$$\frac{dP}{dT} = \frac{dP}{dT_{dew}} \times \frac{dT_{dew}}{dT} \quad (10)$$

91 If relative humidity remains unchanged, we would expect the dew point temperature to increase
92 continuously with surface temperature, representing a moisture increase of 7%/K. However, when dew
93 point temperatures are compared to "all-sky" temperatures (red line, Figure 5c), we note that a break
94 occurs in this scaling as well. Dew point temperatures increase with "all-sky" temperatures for colder
95 temperatures more strongly than what would be expected from an unchanged relative humidity when air
96 gets warmer. However, at temperatures of above 23° - 25°C, dew point temperatures fall, reflecting a
97 decrease in relative humidity that is typical for warm, arid regions. Thus, one does not see a breakdown
98 in precipitation - dew point scaling because the information on the breakdown is contained in how dew
99 point temperatures change with surface air temperatures (second term in equation 10). Similar findings
00 were also reported in Roderick et al (2019).

01 The scaling of dew point temperatures with "clear-sky" temperatures is much more uniform and consistent
02 across the whole temperature range and does not show a breakdown or a super CC scaling in the
03 relationship. This is because the "clear-sky" temperatures reflect the radiative conditions, and not the
04 effects of atmospheric humidity or clouds. In contrast, observed temperatures and "all-sky" temperatures
05 co-vary with cloud effects, which in turn are linked to precipitation and humidity, thus resulting in less
06 clear scaling relationships that are less straightforward to interpret. This further implies that moisture
07 loading of the atmosphere primarily occurs during the non-precipitating periods that are more
08 representative of clear-sky radiative conditions.

09 The breakdown in scaling effect can thus be explained by the cooler temperatures associated with
10 precipitation events. This cooling shifts the precipitation extremes to lower temperature bins while the
11 high-temperature bins then correspond to more arid regions or to the drier pre-monsoon season
12 temperatures with lower values of precipitation extremes. We refer to this as a “bin-shifting” effect. The
13 cooling effect is proportional to the amount of precipitation (Fig. 3A) and hence, the heavier the
14 precipitation, the stronger the cooling and bin shifting becomes. When the cloud cooling effect is
15 removed, as in the case of “clear-sky” temperatures, extreme precipitation then shows a scaling that is
16 consistent with the CC rate. This bin shifting effect arising due to the presence of clouds also causes a
17 decrease in relative humidity at higher temperatures. This effect can be seen by the stronger increase in
18 dewpoint temperatures below 25°C, and the decline above this temperature (Figure 5c). The breakdown
19 in scaling is thus not directly related to changes in aridity or moisture availability, but rather to the
20 radiative effect of clouds on surface temperature.

21 To demonstrate the implications of our interpretation for precipitation scaling across regions, we
22 estimated regression slopes of 99th percentile precipitation events for both sub-daily (TRMM) and daily
23 (IMD & APHRODITE) precipitation with the different temperatures using the Quantile Regression
24 method (Wasko et al., 2014). We found that extreme precipitation scaling was negative for both, observed
25 and “all-sky” temperatures over most regions (Figure 6) except for the Himalayan foothills in the North
26 of India. The scaling rates for sub-daily extremes were slightly higher than those estimated for daily
27 extremes but yet remains negative over most grids. When the cooling effect of clouds is removed by using
28 “clear-sky” temperatures, extreme precipitation scaling then shows a diametric change and scaling
29 estimates come close to CC rates over most of the regions. A similar diametric change in the scaling was
30 also obtained with the APHRODITE precipitation dataset (Appendix B). The highest positive sensitivities
31 were found over the Central Indian region where a widespread increase in rainfall extremes is already
32 reported (Roxy et al., 2017). There seems to be a minor difference between the clear sky scaling in IMD
33 and TRMM in foothill of Himalayas north of India, which is likely because of the underestimation of
34 rainfall by TRMM over this region (Sharma et al., 2020; Shukla et al., 2019).

35 We also note that negative scaling was found over few regions of South-central and south-east India with
36 “clear-sky” temperatures at both daily and sub-daily scales (Figure 6 c,f). To our understanding, this

Deleted: also

38 negative scaling primarily arises due to two reasons. Firstly, these are the grids which receives
39 contribution from rainfall during both summer and winter monsoon. However, a relatively higher
40 proportion of the rain happens during winter monsoon (Figure C1). The reason being that this region lies
41 over the leeward side of Western ghats for the incoming southwest monsoon winds during summer
42 monsoon. Whereas during the winter monsoon, Northeast winds blow over Bay of Bengal leading to large
43 moisture advection and more rain over this region. As a result of this seasonality effect more extreme
44 precipitation are sampled during winter season over this region while during the summer season, moisture
45 supply may limit these extremes to increase. This may lead to a negative scaling when a single quantile
46 regression slope is fitted over the whole temperature range. Another reason could be the development of
47 low-pressure system in Bay of Bengal during winter months which causes cyclones over the Eastern coast
48 of India. These cyclonic systems cause very high rainfall at very low temperatures which can lead to
49 negative scaling (Traxl et al., 2021). More work is needed to be done to resolve these systems in
50 conventional scaling approach and remains an important area for future research.

51 The effect of seasonality on precipitation scaling was also checked by producing the scaling curves for
52 different seasonal subsets (summer and winter monsoon). We find a change in scaling during summer
53 season after removing the cloud effects as the drop disappears (See Appendix C). Winter season on the
54 other hand is associated with reduced rainfall amounts (less than 20%) and less clouds over most regions
55 resulting in a similar scaling for both “all-sky” and “clear-sky” temperatures.

56 While there exist some differences, cloud cooling effect largely explains the negative scaling over most
57 of the grid points over India. Extreme precipitation increases monotonically with temperature when the
58 cloud cooling effect is removed. This implies that the “peak-structures” obtained with observed scaling
59 will not constrain the rise in extremes with anthropogenic warming. The confounding effect between
60 precipitation and temperature on observed scaling relationships, also termed as “apparent scaling” had
61 also been argued by some recent studies (Bao et al. 2017; Visser et al., 2020). Our results agree with these
62 studies that the observed scaling relationships also reflect the impact of synoptic conditions and cooling
63 associated with precipitation events on temperature. However, we suggest that this confounding effect is
64 largely associated with cloud radiative effect, which is removed by our use of “clear-sky” temperatures
65 as a scaling variable. We also address the arguments raised to resolve apparent scaling using dew point

Deleted: i

Deleted: s largely due to the cyclonic activities originating from Bay of Bengal during winter months and resulting in heavy rains over these regions.

Deleted: thus

Deleted: uses

Deleted: .

Deleted: Our findings indicate that seasonality does have an effect on observed scaling while the “clear-sky” scaling rates remains positive irrespective of the seasons (see Appendix C).

Formatted: Font colour: Accent 1

Deleted:

77 temperature (Barbero et al., 2018). Our results confirm that precipitation extremes scale well with dew
78 point temperatures as a measure for atmospheric moisture, but that the break in scaling actually originates
79 from the scaling of dew point temperatures with observed temperatures. This response of dew point
80 temperature to warming is further affected by the presence of clouds and associated radiative cooling.
81 "Clear-sky" temperatures are independent of the co-variations arising from cloud effects and are thus a
82 better, more independent measure and scaling variable to understand the precipitation response to climate
83 warming.

84 **4 Summary and Conclusions**

85 We showed that the observed negative scaling of extreme precipitation in India arises mostly from the
86 cloud radiative cooling of surface temperatures. When this effect is removed, we get a positive scaling
87 consistent with the CC rate. Scaling rates estimated from observed temperatures are thus likely to
88 misrepresent the response of extreme precipitation to global warming, because the cooling effects of
89 clouds make precipitation and temperature covary with each other. When this effect is removed by
90 estimating surface temperatures for "clear-sky" conditions, the scaling relationships with moisture content
91 and precipitation become much clearer and confirm the CC scaling of extreme precipitation events with
92 warmer temperatures. This explains the apparent discrepancy between the observed negative scaling rates
93 over India and the projected increase in precipitation extremes by climate models.

94 While the scaling with "clear-sky" temperatures shows a diametric change and significant improvement
95 over observed scaling, there still exist regional variabilities in scaling rates and deviations from CC
96 scaling (7%/K). We believe that these deviations could be due to the following reasons. Firstly, present
97 scaling approach does not explicitly consider the contribution from the large-scale dynamics and regional
98 circulation patterns which can cause local changes in the scaling estimates. The effect of change in rainfall
99 types - Orographic, stratiform or convective is not accounted for and it can affect the estimates of scaling
00 rates. Lastly, Inconsistencies between precipitation and radiation datasets can also cause uncertainties in
01 estimating the cooling associated with rainfall event and can affect the estimates of scaling rates.

02 It is also important to note that the goal of our study was not to compare the accuracy of scaling estimates
03 from different gridded and station-based datasets, but rather to identify and remove the physical effects

04 that causes uncertainties in this response. Our methodology to remove the cooling effect of clouds from
05 surface temperatures significantly improves the scaling estimate for daily precipitation scaling.

06 While our study was confined over the Indian region, we would expect that cloud effects on surface
07 temperatures can explain the deviations in precipitation scaling from CC rates in other tropical regions
08 too. Furthermore, our methodology to remove the cloud cooling effects on surface temperatures could be
09 extended to derive scaling relationships of other, observed variables to obtain their response to global
10 warming as well. Our findings add a novel component to better interpret precipitation scaling rates derived
11 from observations to support climate model projections.

12 **Data Availability**

13 The daily gridded precipitation and temperature datasets were obtained from the Indian Meteorological
14 department (IMD, https://cdsp.imdpune.gov.in/home_gridded_data.php (doi: 10.1029/2008GL035143)).

15 The APHRODITE (Asian Precipitation Highly Resolved Observational Data Integration towards
16 Evaluation) dataset is available at <http://aphrodite.st.hirosaki-u.ac.jp/products.html>. Sub-daily
17 precipitation data at 3 hourly resolution was obtained from TRMM (Tropical Rainfall measuring mission)
18 TMPA_3B42_V7 data (doi: 10.5067/TRMM/TMPA/3H/7)
19 https://disc.gsfc.nasa.gov/datasets/TRMM_3B42_7/summary. Station-based daily precipitation -
20 temperature data was taken from NOAA – GSOD sites (Station id: 43295099999, 43003099999 and
21 43279099999) at <https://www.ncei.noaa.gov/access/search/data-search/global-summay-of-the-day>.

22 Surface and TOA gridded radiative flux datasets are obtained from NASA CERES EBAF data (doi:
23 https://doi.org/10.5067/Terra-Aqua/CERES/EBAF_L3B.004.1) and NASA CERES Syn1deg data (doi:
24 [10.5067/TERRA+AQUA/CERES/SYN1DEG-1HOUR_L3.004A](https://doi.org/10.5067/TERRA+AQUA/CERES/SYN1DEG-1HOUR_L3.004A)) at <https://ceres.larc.nasa.gov/data/>.
25 Daily dew point temperature data is obtained from the ERA-5 reanalysis (doi: 10.24381/cds.e2161bac).

26 **Acknowledgements**

27 The author thanks the NASA CERES team for making the satellite data openly available (doi:
28 [10.5067/Terra-Aqua/CERES/EBAF_L3B.004.1](https://doi.org/10.5067/Terra-Aqua/CERES/EBAF_L3B.004.1) and [10.5067/TERRA+AQUA/CERES/SYN1DEG-](https://doi.org/10.5067/TERRA+AQUA/CERES/SYN1DEG-1HOUR_L3.004A)

29 1HOUR_L3.004A) and the Copernicus Climate Change Service for the access to the ERA-5 reanalysis
30 data (doi: 10.24381/cds.e2161bac).

31 **Author Contribution**

32 All the authors contributed to the idea and development of the hypothesis. SAG carried out the data
33 analysis. The writing of the manuscript was done by SAG with inputs and edits from AK. AK and SG
34 helped in designing the study. All the authors contributed to the interpretation of the results.

35 **References**

- 36 1. Acero, F., García, J., & Gallego, M. (2011). Peaks-over-Threshold Study of Trends in Extreme
37 Rainfall over the Iberian Peninsula. *Journal of Climate*, 24(4), 1089-1105. Retrieved May 31,
38 2021, from <http://www.jstor.org/stable/26190418>
- 39 2. Ali, H., Fowler, H. J., Lenderink, G., Lewis, E., & Pritchard, D. (2021). Consistent large-scale
40 response of hourly extreme precipitation to temperature variation over land. *Geophysical*
41 *Research Letters*, 48, e2020GL090317. <https://doi.org/10.1029/2020GL090317>
- 42 3. Allen, M., Ingram, W. Constraints on future changes in climate and the hydrologic cycle.
43 *Nature* 419, 228–232 (2002). <https://doi.org/10.1038/nature01092>
- 44 4. Ban, N., J. Schmidli, and C. Schär (2015), Heavy precipitation in a changing climate: Does
45 short-term summer precipitation increase faster?, *Geophys. Res. Lett.*, 42, 1165–1172,
46 doi:10.1002/2014GL062588.
- 47 5. Bao, J., Sherwood, S. C., Alexander, L. V. & Evans, J. P. Comments on “temperature-extreme
48 precipitation scaling: A two-way causality?”. *Int. J. Climatol.* 38, 4661–4663 (2018).
- 49 6. Bao, J., Sherwood, S., Alexander, L. et al. Future increases in extreme precipitation exceed
50 observed scaling rates. *Nature Clim Change* 7, 128–132 (2017).
51 <https://doi.org/10.1038/nclimate3201>
- 52 7. Barbero, R., Westra, S., Lenderink, G. & Fowler, H. J. Temperature-extreme precipitation
53 scaling: a two-way causality? *Int. J. Climatol.* 38, e1274–e1279 (2018).

- 54 8. Berg, P., Moseley, C., & Haerter, J. O. (2013). Strong increase in convective precipitation in
55 response to higher temperatures. *Nature Geoscience*, 6(3), 181–185.
56 <https://doi.org/10.1038/ngeo1731>
- 57 9. Bui A, Johnson F and Wasko C 2019 The relationship of atmospheric air temperature and dew
58 point temperature to extreme rainfall *Environ. Res. Lett.* 14 074025
- 59 10. Chan, S.C., Kendon, E.J., Roberts, N.M., Fowler, H.J. and Blenkinsop, S. (2015) Downturn
60 in scaling of UK extreme rainfall with temperature for future hottest days. *Nature Geoscience*,
61 9(1), 24– 28. <https://doi.org/10.1038/ngeo2596>.
- 62 11. Dhara, C., Renner, M., & Kleidon, A. (2016). Broad climatological variation of surface energy
63 balance partitioning across land and ocean predicted from the maximum power limit.
64 <https://doi.org/10.1002/2016GL070323.1>.
- 65 12. Doelling DR, Loeb NG, Keyes DF, Nordeen ML, Morstad D, Nguyen C, Sun M (2013)
66 Geostationary enhanced temporal interpolation for CERES flux products. *J Atmos Oceanic*
67 *Technol* 30(6):1072–1090
- 68 13. Doelling DR, Sun M, Nguyen LT, Nordeen ML, Haney CO, Keyes DF, Mlynchak PE (2016)
69 Advances in geostationary-derived longwave fluxes for the CERES synoptic (SYN1 deg)
70 product. *J Atmos Oceanic Technol* 33(3):503–521
- 71 14. Donat, M. G., Lowry, A. L., Alexander, L. V., O’Gorman, P. A. & Maher, N. More extreme
72 precipitation in the world’s dry and wet regions. *Nat. Clim. Change* 6, 508–513 (2016)
- 73 15. Fischer, E. M., Beyeler, U. & Knutti, R. Robust spatially aggregated projections of climate
74 extremes. *Nat. Clim. Change* 3, 1033–1038 (2013).
- 75 16. Gao, X., Zhu, Q., Yang, Z., Liu, J., Wang, H., Shao, W., & Huang, G. (2018). Temperature
76 Dependence of Hourly, Daily, and Event-based Precipitation Extremes Over China. *Scientific*
77 *Reports*, 8(1), 1–10. <https://doi.org/10.1038/s41598-018-35405-4>
- 78 17. Ghauri, S. A., & Ghosh, S. (2020). Diametrically Opposite Scaling of Extreme Precipitation
79 and Stream flow to Temperature in South and Central Asia, 1–10.
80 <https://doi.org/10.1029/2020GL089386>

- 81 18. Golroudbary, V. R., Zeng, Y., Mannaerts, C. M., & Su, Z. (2019). Response of extreme
82 precipitation to urbanization over the Netherlands. *Journal of Applied Meteorology and*
83 *Climatology*, 58(4), 645–661. <https://doi.org/10.1175/jamc-d-18-0180.1>
- 84 19. Goswami, B. N., Venugopal, V., Sengupta, D., Madhusoodanan, M. S. & Xavier, P. K. (2006).
85 Increasing trend of extreme rain events over India in a warming environment. *Science* 314,
86 1442–5. DOI: 10.1126/science.1132027
- 87 20. Hardwick Jones, R., Westra, S., & Sharma, A. (2010). Observed relationships between
88 extreme sub-daily precipitation, surface temperature, and relative humidity. *Geophysical*
89 *Research Letters*, 37(22), 1–5. <https://doi.org/10.1029/2010GL045081>
- 90 21. Held, I. M. and Soden, B. J.: Robust responses of the hydrological cycle to global warming, *J.*
91 *Climate*, 19, 5686–5699, 2006.
- 92 22. Kato, S., F. G. Rose, D. A. Rutan, T. E. Thorsen, N. G. Loeb, D. R. Doelling, X. Huang, W.
93 L. Smith, W. Su, and S.-H. Ham, 2018: Surface irradiances of Edition 4.0 Clouds and the
94 Earth’s Radiant Energy System (CERES) Energy Balanced and Filled (EBAF) data product,
95 *J. Climate*, 31, 4501–4527, doi:10.1175/JCLI-D-17-0523.1
- 96 23. Katzenberger, A.; Schewe, J.; Pongratz, J.; Levermann, A. Robust increase of Indian monsoon
97 rainfall and its variability under future warming in CMIP-6 models. *Earth Syst. Dyn.* 2020.
- 98 24. Kendon, E. J., Roberts, N. M., Fowler, H. J., Roberts, M. J., Chan, S. C., & Senior, C. A.
99 (2014). Heavier summer downpours with climate change revealed by weather forecast
00 resolution model. *Nature Climate Change*, 4(7), 570–576.
01 <https://doi.org/10.1038/nclimate2258>
- 02 25. Kleidon, A., & Renner, M. (2013). A simple explanation for the sensitivity of the hydrologic
03 cycle to climate change. *Earth System Dynamics*, 4(2), 455–465. [https://doi.org/10.5194/esd-](https://doi.org/10.5194/esd-4-455-2013)
04 [4-455-2013](https://doi.org/10.5194/esd-4-455-2013)
- 05 26. Kleidon, A., Renner, M., & Porada, P. (2014). Estimates of the climatological land surface
06 energy and water balance derived from maximum convective power. *Hydrology and Earth*
07 *System Sciences*, 18, 2201–2218. <https://doi.org/10.5194/hess-18-2201-2014>

- 08 27. Lenderink, G., & Van Meijgaard, E. (2008). Increase in hourly precipitation extremes beyond
09 expectations from temperature changes. *Nature Geoscience*, 1(8), 511–514.
10 <https://doi.org/10.1038/ngeo262>
- 11 28. Loeb, N. G., Doelling, D. R., Wang, H., Su, W., Nguyen, C., Corbett, J. G., Liang, L.,
12 Mitrescu, C., Rose, F. G., and Kato, S.: Clouds and the Earth's Radiant Energy System
13 (CERES) Energy Balanced and Filled (EBAF) Top-of-Atmosphere (TOA) Edition-4.0 data
14 product, *J. Climate*, 31, 895–918, <https://doi.org/10.1175/JCLI-D-17-0208.1>, 2018.
- 15 29. Molnar, P., Faticchi, S., Gaál, L., Szolgay, J., & Burlando, P. (2015). Storm type effects on
16 super Clausius-Clapeyron scaling of intense rainstorm properties with air temperature.
17 *Hydrology and Earth System Sciences*, 19(4), 1753–1766. [https://doi.org/10.5194/hess-19-](https://doi.org/10.5194/hess-19-1753-2015)
18 [1753-2015](https://doi.org/10.5194/hess-19-1753-2015)
- 19 30. Mukherjee S, Saran A, Stone D, Mishra V (2018) Increase in extreme precipitation events
20 under anthropogenic warming in India. *Weather Clim Extrem* 20:45–53.
21 <https://doi.org/10.1016/j.wace.2018.03.005>
- 22 31. O’Gorman, P. A. & Schneider, T. The physical basis for increases in precipitation extremes
23 in simulations of 21st-century climate change. *Proc. Natl Acad. Sci. USA* 106, 14773–14777
24 (2009).
- 25 32. Rajeevan, M., Jyoti Bhate, A.K.Jaswal : Analysis of variability and trends of extreme rainfall
26 events over India using 104 years of gridded daily rainfall data., , 2008, *Geophysical Research*
27 *Letters*, Vol.35, L18707, doi:10.1029/2008GL035143.
- 28 33. Roderick TP, Wasko C, Sharma A. 2019 Atmospheric moisture measurements explain
29 increases in tropical rainfall extremes. *Geophys. Res. Lett.* 46, 1375–1382.
30 (doi:10.1029/2018GL080833)
- 31 34. Roxy, M. K., Ghosh, S., Pathak, A., Athulya, R., Mujumdar, M., Murtugudde, R., ...
32 Rajeevan, M. (2017). A threefold rise in widespread extreme rain events over central India.
33 *Nature Communications*, 8(1), 1–11. <https://doi.org/10.1038/s41467-017-00744-9>

- 34 35. Schroeer, K., & Kirchengast, G. (2018). Sensitivity of extreme precipitation to temperature:
 35 the variability of scaling factors from a regional to local perspective. *Climate Dynamics*,
 36 50(11), 3981–3994. <https://doi.org/10.1007/s00382-017-3857-9>
- 37 36. Sharma, S., & Mujumdar, P. P. (2019). On the relationship of daily rainfall extremes and local
 38 mean temperature. *Journal of Hydrology*, 572(September 2018), 179–191.
 39 <https://doi.org/10.1016/j.jhydrol.2019.02.048>
- 40 37. Sharma, S., Khadka, N., Hamal, K., Shrestha, D., Talchabhadel, R., & Chen, Y. (2020). How
 41 accurately can satellite products (TMPA and IMERG) detect precipitation patterns,
 42 extremities, and drought across the Nepalese Himalaya?. *Earth and Space Science*, 7,
 43 e2020EA001315. <https://doi.org/10.1029/2020EA001315>
- 44 38. Shukla AK, Ojha CSP, Singh RP, Pal L, Fu D. Evaluation of TRMM Precipitation Dataset
 45 over Himalayan Catchment: The Upper Ganga Basin, India. *Water*. 2019; 11(3):613.
 46 <https://doi.org/10.3390/w11030613>
- 47 39. Sun, Q., Zwiers, F., Zhang, X. & Li, G. A comparison of intra-annual and long-term trend
 48 scaling of extreme precipitation with temperature in a large-ensemble regional climate
 49 simulation. *J. Clim.* 33, 9233–9245 (2020).
- 50 40. Traxl, D., Boers, N., Rheinwalt, A. *et al.* The role of cyclonic activity in tropical temperature-
 51 rainfall scaling. *Nat Commun* 12, 6732 (2021). <https://doi.org/10.1038/s41467-021-27111-z>
- 52 41. Trenberth, K. E., Dai, A., Rasmussen, R. M., & Parsons, D. B. (2003). The changing character
 53 of precipitation. *Bulletin of the American Meteorological Society*, 84(9), 1205–1217+1161.
 54 <https://doi.org/10.1175/BAMS-84-9-1205>
- 55 42. Utsumi, N., Seto, S., Kanae, S., Maeda, E. E., & Oki, T. (2011). Does higher surface
 56 temperature intensify extreme precipitation? 38(June), 1–5.
 57 <https://doi.org/10.1029/2011GL048426>
- 58 43. Visser, J. B., Wasko, C., Sharma, A., & Nathan, R. (2020). Resolving Inconsistencies in
 59 Extreme Precipitation-Temperature Sensitivities. *Geophysical Research Letters*, 47(18),
 60 e2020GL089723. <https://doi.org/10.1029/2020GL089723>

Formatted: Font: (Default) +Body (Times New Roman), 12 pt

Formatted: Normal (Web), Justified, Line spacing: 1,5 lines

Formatted: Font: (Default) +Body (Times New Roman)

Formatted: Font: (Default) +Body (Times New Roman), 12 pt

Formatted: Border: Top: (No border), Bottom: (No border), Left: (No border), Right: (No border), Between : (No border)

Formatted: Font: (Default) +Body (Times New Roman),

Formatted: English (US)

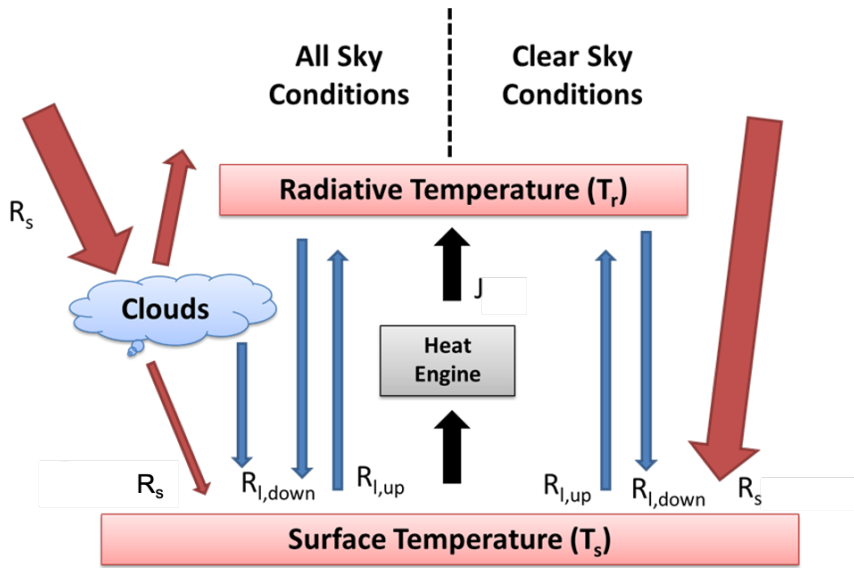
Formatted: Border: Top: (No border), Bottom: (No border), Left: (No border), Right: (No border), Between : (No border)

Formatted: Font: (Default) +Body (Times New Roman),

- 61 44. Visser, Johan B., Conrad Wasko, Ashish Sharma, and Rory Nathan. "Eliminating the "Hook"
62 in Precipitation–Temperature Scaling", *Journal of Climate* 34, 23 (2021): 9535-9549, accessed
63 Nov 10, 2021, <https://doi.org/10.1175/JCLI-D-21-0292.1>
- 64 45. Vittal, H., Ghosh, S., Karmakar, S. et al. Lack of Dependence of Indian Summer Monsoon
65 Rainfall Extremes on Temperature: An Observational Evidence. *Sci Rep* 6, 31039 (2016).
66 <https://doi.org/10.1038/srep31039>
- 67 46. Wang, G., Wang, D., Trenberth, K. et al. The peak structure and future changes of the
68 relationships between extreme precipitation and temperature. *Nature Clim Change* 7, 268–274
69 (2017). <https://doi.org/10.1038/nclimate3239>
- 70 47. Wasko, C., & Sharma, A. (2014). Quantile regression for investigating scaling of extreme
71 precipitation with temperature. *Water Resources Research*, 50(4), 3608–3614.
72 <https://doi.org/10.1002/2013WR015194>
- 73 48. Wasko, C., Lu, W. T., & Mehrotra, R. (2018). Relationship of extreme precipitation, dry-bulb
74 temperature, and dew point temperature across Australia. *Environmental Research Letters*,
75 13(7). <https://doi.org/10.1088/1748-9326/aad135>
- 76 49. Westra, S., Alexander, L. V., & Zwiers, F. W. (2013). Global increasing trends in annual
77 maximum daily precipitation. *Journal of Climate*, 26(11), 3904–3918.
78 <https://doi.org/10.1175/JCLI-D-12-00502.1>
- 79 50. Westra, S., Fowler, H. J., Evans, J. P., Alexander, L. V., Berg, P., Johnson, F., et al. (2014).
80 Future changes to the intensity and frequency of short-duration extreme rainfall. *Rev.*
81 *Geophys.* 52, 522–555. doi: 10.1002/2014RG000464
- 82 51. Yatagai, A., Kamiguchi, K., Arakawa, O., Hamada, A., Yasutomi, N., & Kitoh, A. (2012).
83 Aphrodite constructing a long-term daily gridded precipitation dataset for Asia based on a
84 dense network of rain gauges. *Bulletin of the American Meteorological Society*, 93(9), 1401–
85 1415. <https://doi.org/10.1175/BAMS-D-11-00122.1>
- 86 52. Zhang, W., Villarini, G., & Wehner, M. (2019). Contrasting the responses of extreme
87 precipitation to changes in surface air and dew point temperatures. *Climatic Change*, 154(1–
88 2), 257–271. <https://doi.org/10.1007/s10584-019-02415-8>

89

90 Figures:



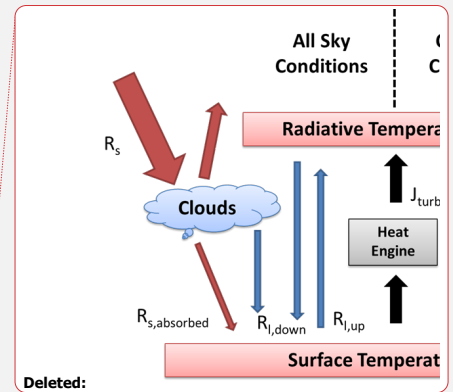
91

92 Figure 1. Schematic diagram of the surface energy balance, the fluxes of solar (red) and terrestrial
 93 (blue) radiation, as well as the turbulent heat fluxes (black). We consider turbulent heat exchange
 94 being driven primarily by an atmospheric heat engine that operates at the thermodynamic limit of
 95 maximum power.

96

97

98



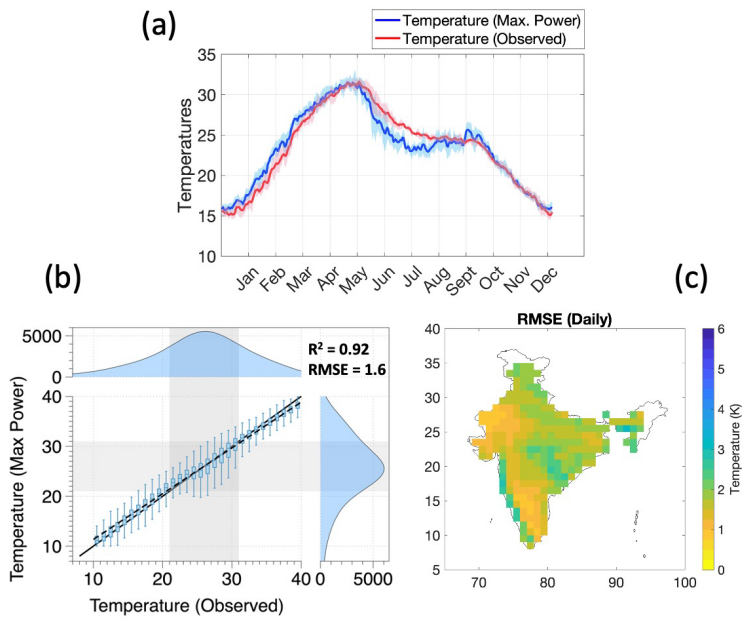
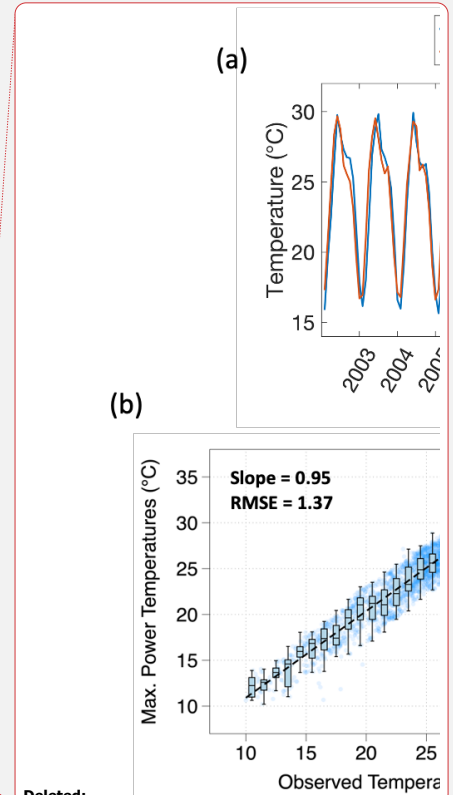
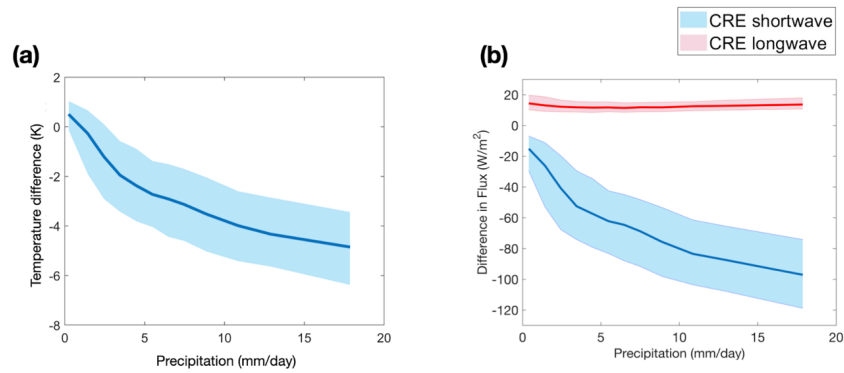


Figure 2: Comparison of daily annual cycle of temperature for observed (IMD) and estimated “all-sky” surface temperatures, averaged over all grid points. (B) Regression between the two temperatures at the grid-point scale. (C) Spatial variation of the root mean squared error (RMSE) in temperature estimates from maximum power compared to observed temperatures.

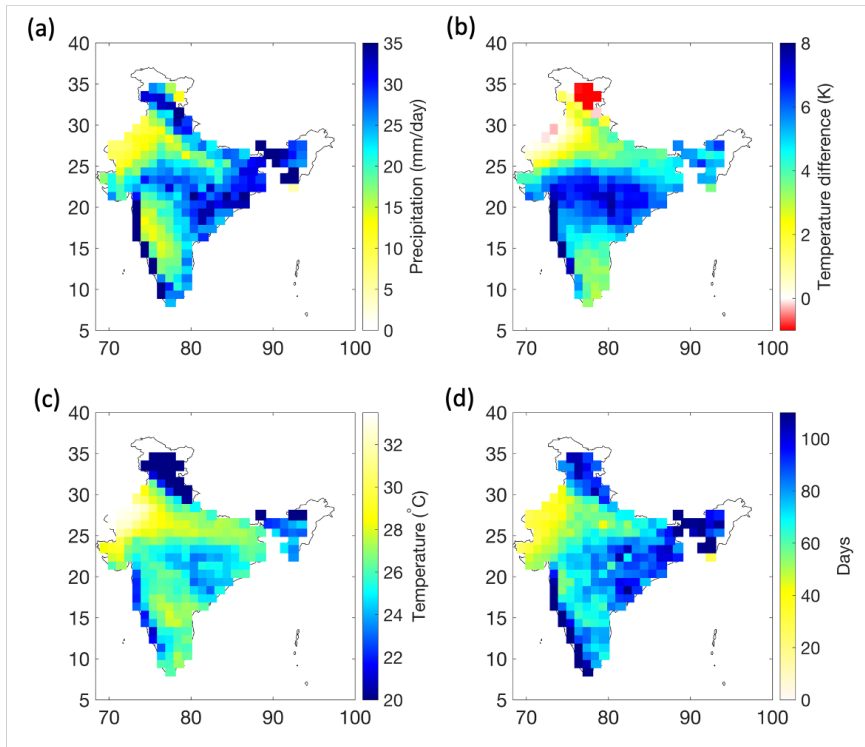


Deleted:

Deleted: Figure 2: Comparison of monthly mean temperature time series for observed (IMD) and estimated “all-sky” surface temperatures, averaged over all grid points. (B) Regression between the two temperatures at the grid-point scale. (C) Spatial variation of the root mean squared error (RMSE) in temperature estimates from maximum power compared to observed temperatures....



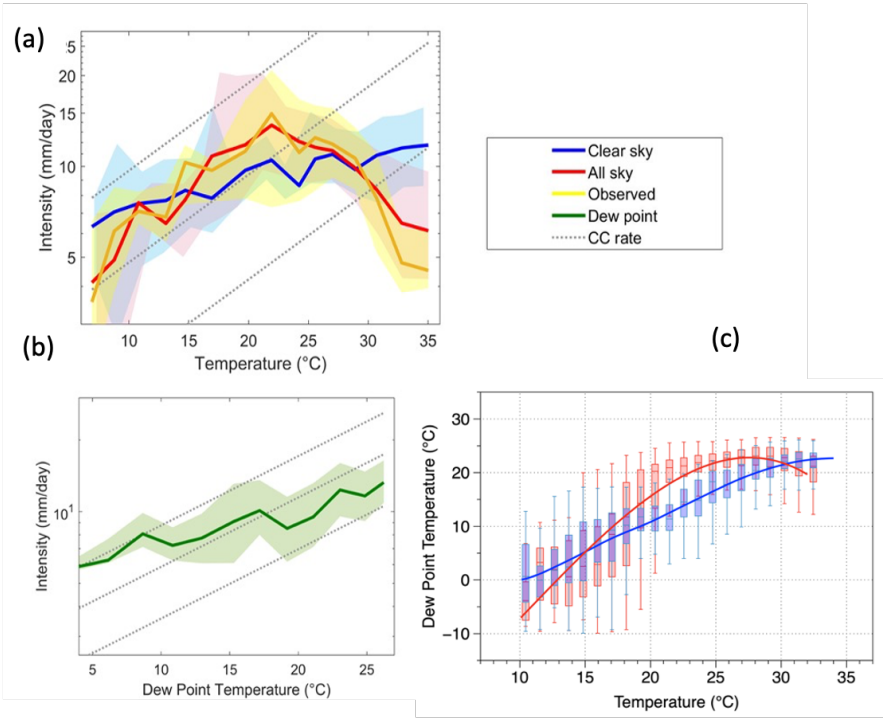
16 **Figure 3: (a) Cooling effect of clouds on surface temperatures calculated from the difference of "all-**
 17 **sky" to "clear-sky" surface temperatures as a function of precipitation over the Indian region.**
 18 **(b) Difference in net shortwave and downwelling longwave radiative fluxes ("Cloud Radiative**
 19 **Effect", CRE) between "all-sky" and "clear-sky" radiative conditions at the surface as a**
 20 **function of precipitation. This was inferred using NASA – CERES (EBAF ed4.1) dataset (Loeb**
 21 **et al., 2018).**



23

24 **Figure 4. Regional variation of (a) mean daily extreme precipitation (99th percentile) (b) the**
 25 **temperature difference between "clear-sky" and "all-sky" radiative conditions averaged during**
 26 **extreme precipitation events (c) "All-sky" surface temperature during the occurrence of the event**
 27 **(d) Mean number of rainfall days per year**

28

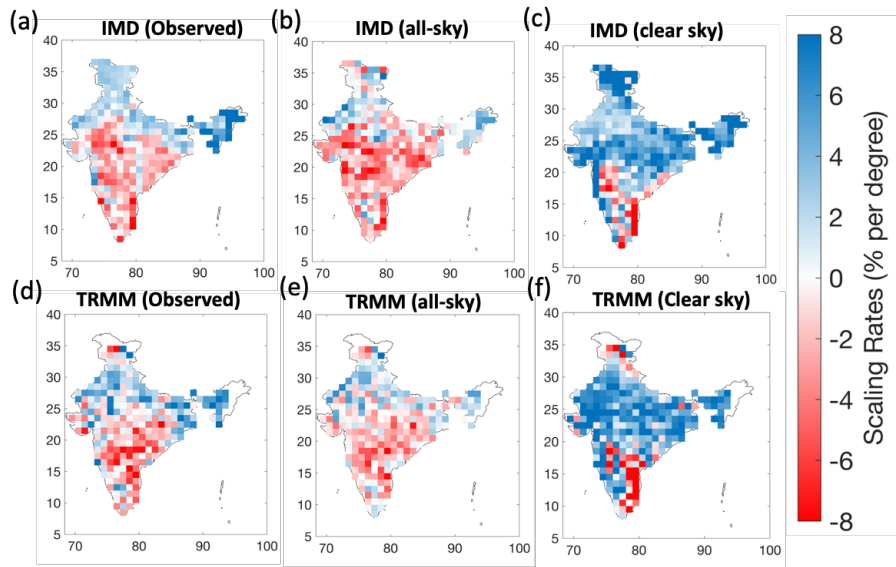


29

30

31 **Figure 5. (a) Extreme precipitation-temperature scaling using observed (yellow), "all-sky" (red)**
 32 **and "clear-sky" (blue) temperatures over India. (b) Same as (a), but using dew point**
 33 **temperatures. (c) Relationship between dew point temperatures and "all-sky" (red) and**
 34 **"clear-sky" (blue) temperatures. The shaded areas represent the variance in terms of the**
 35 **interquartile range for each bin. Grey dotted lines indicate the Clausius-Clapeyron scaling**
 36 **rate. Note: Logarithmic vertical axis for figure (a,b)**

37



38

39 **Figure 6. Regional variation of 99th percentile precipitation-temperature scaling rates using daily**
 40 **(a-c) and 3 hourly (d -f) rainfall data with observed temperatures (a, d), "all-sky" temperatures**
 41 **(b, e) and "clear-sky" temperatures (c, f).**

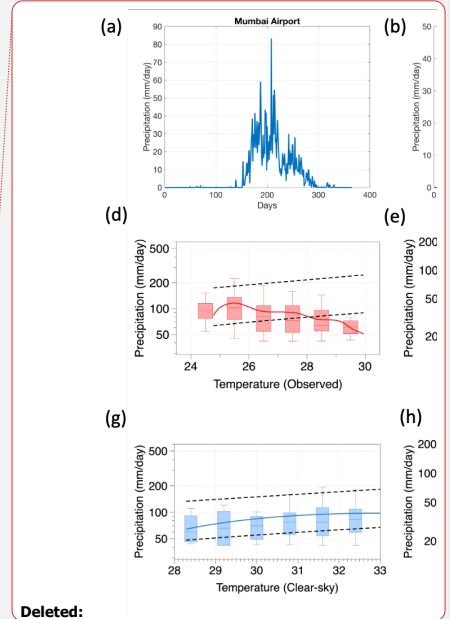
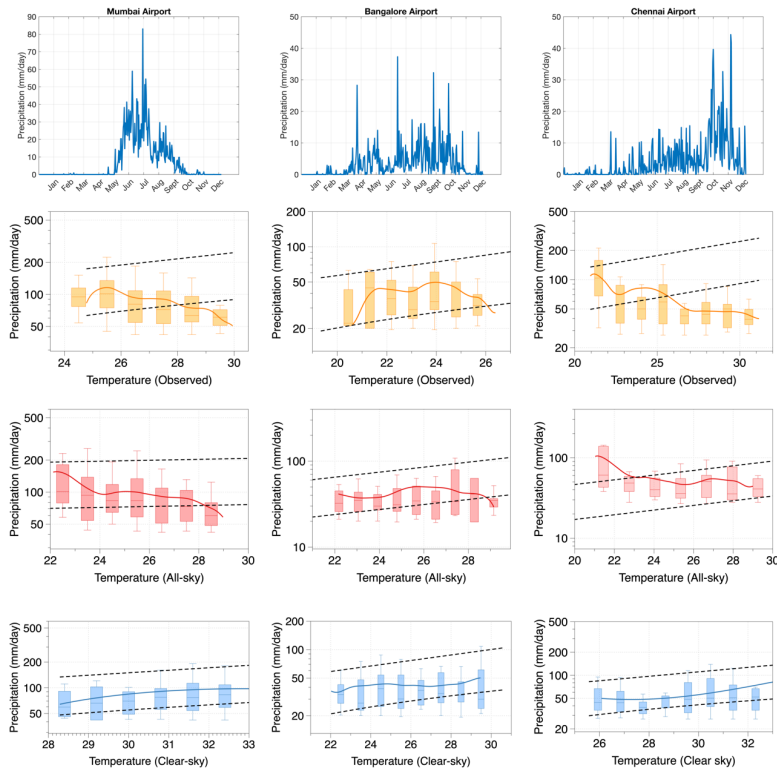
42

43 **Appendix A: Validation of scaling results using station-based GSOD data**

44 We used three station-based daily observations from global surface summary of the day (GSOD) data
45 provided by National Oceanic and Atmospheric Administration (NOAA). We used the data at Mumbai,
46 Chennai and Bangalore Airport to produce the scaling curves (Appendix A). The choice of the station
47 was based to ensure the robustness of results using gauge data as well as to check the effect of seasonality
48 as the three sites receive rainfall during different period of the years. In Mumbai, rainfall occurs mainly
49 during the summer monsoon season while in Chennai heavy rainfall occurs during the winter months
50 (November and December). On other hand, Bangalore receives rainfall during both summer and winter
51 monsoon season (Fig. A1 ~~row 1~~). Negative scaling was found over these three stations using observed
52 (yellow) and “all-sky” (red) temperatures while with “clear-sky” temperatures (blue), we find positive
53 rates largely consistent with the CC rate.

Deleted: a - c

Deleted: (Fig A1 d - i)



Deleted:

Deleted: Figure A1. (a-c) shows the annual cycle of mean daily precipitation over GSOD sites in Mumbai airport, Bangalore airport and Chennai airport respectively. Extreme precipitation – temperature scaling curves for (d-f) observed temperatures in red and (g-i) “Clear-sky” temperatures in blue are presented for all the three sites. Red/Blue solid lines indicate the LOESS regression lines. Grey dotted lines indicate the Clausius-Clapeyron scaling rate. Note Logarithmic vertical axis.

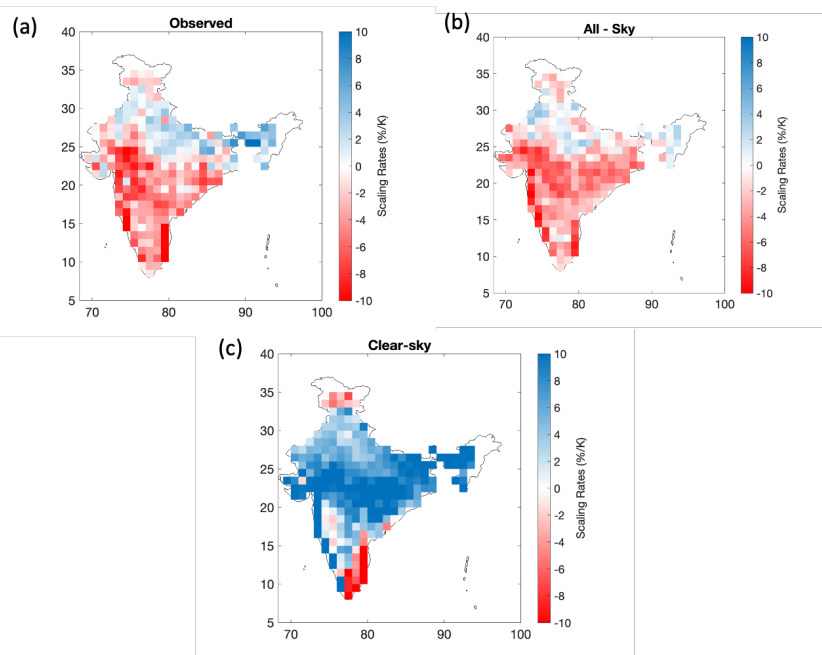
56

57 Figure A1. (Row 1) shows the annual cycle of mean daily precipitation over GSOD sites in Mumbai airport,
 58 Bangalore airport and Chennai airport respectively. Extreme precipitation – temperature scaling curves for
 59 observed temperatures (yellow), “all-sky” temperatures (red) and “Clear-sky” temperatures (in blue) are
 60 presented for all the three sites. Yellow/Red/Blue solid lines indicate the LOESS regression lines. Grey
 61 dotted lines indicate the Clausius-Clapeyron scaling rate. Note Logarithmic vertical axis.

62

72 **Appendix B: Validation of scaling results using APHRODITE dataset**

73 Figure B1 shows the spatial variation of daily precipitation – temperature scaling rates estimated from
74 quantile regression (similar to Fig. 6 in the main text) using the APHRODITE (Asian Precipitation –
75 Highly Resolved Observational Data Integration towards Evaluation of water resources) dataset (Yatagai
76 et al., 2012). The results show a diametric change in scaling from being negative for observed and “all-
77 sky” temperatures to coming close to CC rate (7%/K) for “clear-sky” temperatures. The findings were
78 consistent with that obtained using the IMD and TRMM dataset (Figure 6).



79

80 **Figure B1. Regional variation of 99th percentile daily precipitation-temperature scaling rates using (a)**
81 **Observed (b) “all-sky” and (c) “clear-sky” temperatures. Note: Precipitation data is from APHRODITE**

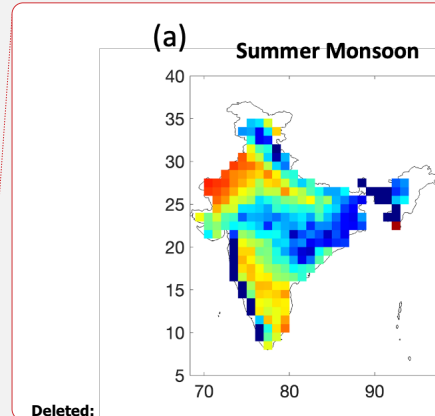
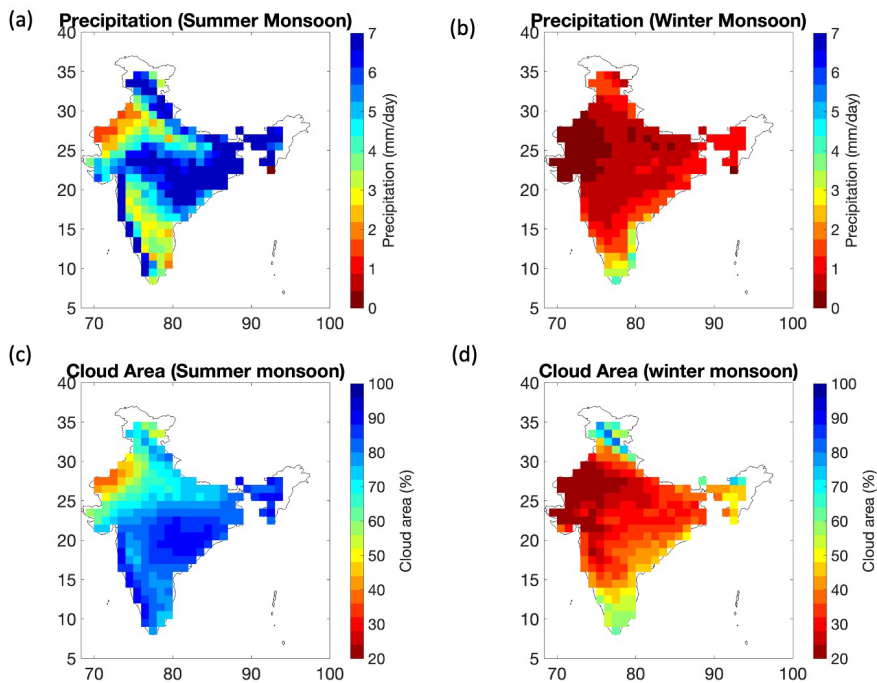
82

83

84 **Appendix C: Effect of seasonality on scaling rates**

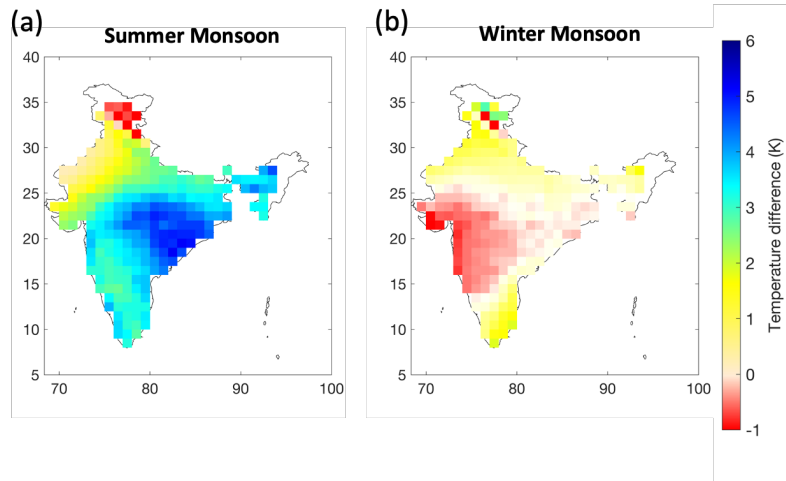
85 To understand the role of seasonality on precipitation – temperature scaling. We divided the precipitation
86 period into two seasonal subsets i.e., summer monsoon season (April to September) and winter monsoon
87 (October to March). Season wise scaling curves (estimated using LOESS regression) are presented in
88 figure C3. We find that observed scaling is uniformly negative in summer over Indian region while during
89 winter the scaling is positive (Fig C3-a, d). This is not surprising because the “hook” or breakdown in
90 scaling happens at high temperature which leads to negative scaling in summer (Figure 5a). Reconstructed
91 “All-sky” temperature showed scaling pattern consistent with observations (Fig. C3- b,e). When scaled
92 with “clear-sky” temperatures, we observed a change in scaling for summer as it turns positive and come
93 close to CC rate. While for winter the scaling ~~does not change for “clear-sky” temperatures~~. It is also
94 important to note that almost 80% of total rainfall over India occurs during the summer monsoon season
95 (Fig C1). As a result, the cooling effect of clouds is mainly experienced during the summer monsoon
96 (where we observed a change in scaling) while the cooling effect remains less than 1K during the winter
97 season (Fig C2). Thus, one does not see a change in scaling between “all-sky” and “clear-sky” conditions
98 for winter season.

Deleted: remains the same (already positive)



00

01 **Figure C1.** shows the map of mean daily precipitation (from IMD) and cloud area fraction (from NASA-
 02 CERES) during (a,c) summer monsoon (April – September) and during (b,d) winter monsoon (October –
 03 March).

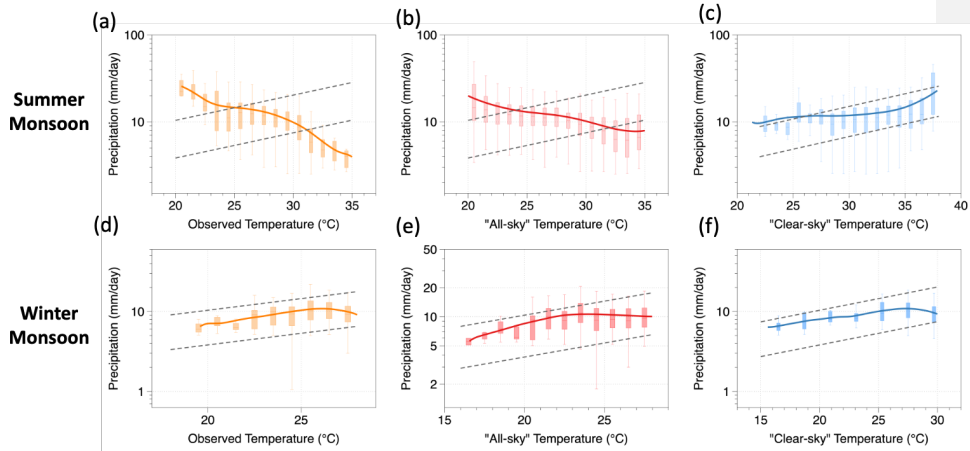


05

06 **Figure C2.** Shows the map of cooling of surface due to clouds (defined as the difference between “clear-sky”
07 and “all-sky” temperatures) for (a) Summer monsoon (April – September) and (b) Winter monsoon
08 (October – March)

09

10



11

12

13 **Figure C3. Extreme precipitation - temperature scaling during summer monsoon (a - c) and winter monsoon**
14 **(d-f). Scaling curves are shown in orange (a,d) for observed temperatures, in red (b,e) for “all-sky”**
15 **temperatures and in blue (c,f) for “clear-sky” temperatures. Orange/red/blue solid lines indicate the LOESS**
16 **regression lines. Grey dotted lines indicate Clausius – Clapeyron scaling rate. Note: Logarithmic vertical**
17 **axis. Dataset used is IMD.**